

Effects of hydrogen absorption on magnetism in Ni₈₀Fe₂₀/Y/Pd trilayers

Charles Weiss^{1,*}, René Hübner,² Martin Saunders,³ Anna Semisalova,^{2,4} Jonathan Ehrler,² Nataliia Schmidt⁵, Johannes Seyd⁵, Manfred Albrecht,⁵ Shadab Anwar^{2,6}, Jürgen Lindner,² Kay Potzger,² and Mikhail Kostylev¹

¹*Department of Physics and Astrophysics, The University of Western Australia, Perth, WA 6009, Australia*


²*Institute of Ion Beam Physics and Materials Research, Helmholtz-Zentrum Dresden-Rossendorf, 01328 Dresden, Germany*

³*Centre for Microscopy, Characterisation and Analysis, The University of Western Australia, Perth, WA 6009, Australia*

⁴*Faculty of Physics and Center for Nanointegration Duisburg-Essen (CENIDE), University of Duisburg-Essen, 47057 Duisburg, Germany*

⁵*Institute of Physics, University of Augsburg, 86159 Augsburg, Germany*

⁶*Technische Universität Dresden, Fakultät Physik, 01062 Dresden, Germany*

 (Received 28 April 2021; revised 5 August 2021; accepted 7 September 2021; published 22 September 2021)

The effects of hydrogen absorption on the effective magnetization ($4\pi M_{\text{eff}}$), gyromagnetic ratio (γ), Gilbert damping constant (α_G), and the inhomogeneous linewidth broadening (ΔH_0) in Py(x)/Y(16 nm)/Pd(15 nm) trilayer films ($x = 2, 3, 5, 8, 10, 20, 40$ nm) were investigated with ferromagnetic resonance (FMR), transmission electron microscopy, and vibrating sample magnetometry. In the presence of a hydrogen atmosphere, the samples show a reduction of their FMR linewidth which is found to stem purely from a reduction of the inhomogeneous linewidth broadening. This is attributed to a rearrangement of atoms at the Py/Y interface in the presence of hydrogen, making the Py/Y interface more homogeneous. In addition, a reduction of $4\pi M_{\text{eff}}$ was seen for all samples in the hydrogen atmosphere which is typical for an increase of the interfacial perpendicular magnetic anisotropy at the Py/Y interface.

DOI: [10.1103/PhysRevB.104.094429](https://doi.org/10.1103/PhysRevB.104.094429)

I. INTRODUCTION

Hydrogen (H₂) gas has become a mainstream contender as an energy and fuel alternative, as there has been a push toward the so-called hydrogen economy [1,2]. Hydrogen is of particular interest for use in fuel cells [1,3] and H₂-fueled cars. With an influx of H₂ usage, in particular in everyday applications, there has been increased research interest in improved hydrogen gas sensors [4,5].

One type of sensor which has gained recent interest is based on a Co/Pd bilayer thin film with perpendicular magnetic anisotropy (PMA) that is excited at ferromagnetic resonance (FMR) [6–10]. In such systems the FMR peak position shifts upon the absorption of hydrogen gas due to a reduction of the PMA [11,12], and thus FMR has become an effective way of probing changes in magnetization dynamics of thin films in the presence of H₂.

When investigating the effects of H₂ on thin-film systems, Pd is typically used as the capping layer due to its strong affinity to reversibly absorb H₂ gas [1]. Furthermore, the rare earth metals lanthanum (La) and yttrium (Y) have also been shown to absorb H₂ [13] at room temperature and atmospheric pressure when interfaced with a Pd capping layer, and this has led to investigations on Fe/Y/Pd [14,15] and Fe/La/Pd [16] repeated multilayer systems. Such systems exhibit similar FMR peak shifts and FMR linewidth narrowing in the presence of H₂ as seen for the Co/Pd system. However, there is limited understanding of the origin of the FMR linewidth narrowing and it has been explained as originating from a reordering of the Fe-Y alloying layer at the Fe/Y interface into

its separate Fe and Y layers [14]. This reordering is referred to as “interface clearing” for the remainder of this paper. Similarly, a reduction of spin pumping would also induce a narrowing of the FMR linewidth [17,18] due to a reduction in the effective Gilbert damping constant and, so far, the origin of the linewidth narrowing in the presence of H₂ has not been investigated.

The aim of this work was to gain further insights into the origin of the FMR linewidth narrowing in the presence of H₂. To achieve this, a series of Py(x)/Y(16 nm)/Pd(15 nm) samples [where Py is permalloy (Ni₈₀Fe₂₀) and $x = 2, 3, 5, 8, 10, 20, 40$ nm] was investigated by means of out of plane (OOP) FMR measurements in order to extract the effective magnetization ($4\pi M_{\text{eff}}$), gyromagnetic ratio (γ), effective Gilbert damping constant (α_G), and the inhomogeneous linewidth broadening (ΔH_0). The OOP geometry was employed, as it simplifies the extraction of $4\pi M_{\text{eff}}$ and γ due to the linear relation of the out of plane Kittel equation, $\omega = \gamma(H_{\text{res}} - 4\pi M_{\text{eff}})$, which governs the FMR in this geometry. Such measurements were carried out in both air and H₂ atmospheres. The FMR measurements were backed up with transmission electron microscopy (TEM) and vibrating sample magnetometry (VSM) measurements in order to examine the thin-film layer structure before hydrogenation and after hydrogen desorption, in particular at the Py/Y interface.

II. EXPERIMENTAL SETUP

A series of Py(x)/Y(16 nm)/Pd(15 nm) samples with $x = 2, 3, 5, 8, 10, 20, 40$ nm was DC sputter deposited on thermally oxidized SiO₂ (100 nm)/Si(100) substrates from Py (99.99%), Y (99.99%), and Pd (99.99%) sputter targets. The Py was deposited first and the Pd was deposited last. In the following,

*charles.weiss@research.uwa.edu.au

these samples are referred to as Py(2 nm) ··· Py(40 nm). For all depositions, a Bestec UHV sputter system (base pressure of $<1 \times 10^{-8}$ mbar) with an Ar work pressure of $5 \mu\text{bar}$ was used. The layer thicknesses were adjusted by the sputtering rates of each target via a calibrated quartz crystal microbalance. The layer thicknesses were further evaluated by Rutherford backscattering spectrometry (RBS). To analyze the Py elemental composition, energy-dispersive x-ray spectroscopy (EDXS) of the sputter target was performed with an EDXS spectrometer and yielded $\text{Ni}_{81}\text{Fe}_{19}$. Further scanning transmission electron microscopy (STEM) based EDXS analysis (for further experimental details see below) of the Py(10 nm) sample yielded a Py layer with an average composition of $\text{Ni}_{82}\text{Fe}_{18}$.

The samples were placed inside a sealable airtight chamber which housed a microstrip line [6] with conductor width of 0.6 mm. The chamber was fixed between the pole pieces of an electromagnet in the out of plane configuration, corresponding to the external field applied perpendicular to the sample plane [19]. A microwave generator and microwave diode were connected to the input and output of the strip line, respectively, and the rectified signal of the microwave diode was fed into a lock-in amplifier, which was referenced by a sine-wave generator oscillating at a frequency of 220 Hz. The signal generator was feeding a small modulation coil which was attached to the outside of the chamber, creating an oscillating magnetic field of ~ 10 Oe perpendicular to the direction of the strip line and parallel with the static magnetic field of the electromagnet. Field-resolved FMR spectra were acquired by setting the microwave driving frequency constant and sweeping the out of plane magnetic field by controlling the current through the electromagnet. A Hall probe was used to measure the strength of the DC magnetic field at the sample location. Due to the field-modulation method, the recorded FMR absorption curves have the shape of the first derivative of a Lorentzian curve (“differential curve”) rather than the typical Lorentzian shape.

The chamber contained two gas ports, with the inlet port connected to a gas mixer, which consisted of two mass flow controllers which allowed for careful mixing of the H_2 and N_2 gases by controlling their individual flow rates. In the presented study, 100% concentration of H_2 and N_2 gases was always used in the chamber, and the gas mixer was solely used to control the flow rates of the gases.

Field-resolved FMR spectra were acquired at various microwave driving frequencies in order to extract the gyromagnetic ratio (γ), effective magnetization ($4\pi M_{\text{eff}}$), effective Gilbert damping constant (α_G), and the inhomogeneous linewidth broadening (ΔH_0), in two atmospheres, 100% air and 100% H_2 . (Note: The FMR spectra do not alter between air and N_2 atmospheres, and thus N_2 was chosen as the carrier gas). During the cycling of atmospheres, time-resolved measurements were carried out to monitor the behavior of the FMR peak shift in real time. This was achieved by setting the driving frequency and static external magnetic field constant onto the FMR peak position (i.e., the steepest part of the differential curve) and recording the time evolution of the lock-in signal. Thus, any shifting of the FMR peak resulted in a sharp increase/decrease of the time-resolved trace, and these measurements were used to qualitatively monitor the absorption

and desorption of hydrogen in the samples. In addition, field-resolved FMR curves were obtained at various time points during the H_2 absorption in order to monitor the absorption rate with respect to time. A flow rate of 800 SCCM (SCCM denotes cubic centimeter per minute at STP) of hydrogen and nitrogen was used during absorption and desorption of the samples, respectively. This was reduced to ~ 50 – 200 SCCM of hydrogen when obtaining field-resolved FMR spectra at various frequencies in the hydrogen atmosphere, in order to conserve hydrogen gas.

In order to better understand the behavior of the atoms at the Py/Y interface in the presence of hydrogen, TEM analysis was carried out on virgin and hydrogenated pieces of Py(2 nm) and Py(10 nm) samples. The sample pieces were cut from the same sputtered sample. One was exposed to the presence of hydrogen, while the other was kept in its virgin state. Due to the TEM analysis being *ex situ* and taken at vacuum pressures, it is expected that the hydrogenated samples no longer contained any hydrogen during the TEM analysis, and thus only permanent, i.e., nonreversible effects of hydrogenation could be investigated with TEM.

For cross-sectional chemical characterization of the thin-film layer stacks, spectrum imaging analysis based on energy-dispersive x-ray spectroscopy (EDXS) was performed in scanning transmission electron microscopy (STEM) mode using a Talos F200X microscope equipped with a high-brightness X-FEG electron source and a Super-X EDX detector system (FEI). Prior to STEM analysis, the specimen, mounted in a high-visibility low-background holder, was placed into a model 1020 plasma cleaner (Fischione) for 8 s to remove possible contamination. Cross-sectional TEM specimen preparation of all samples was done by *in situ* lift-out using a Zeiss Crossbeam NVision 40 system. To protect the sample surface of the layer stack, a carbon cap layer was deposited beginning with electron beam assisted and subsequently followed by Ga focused ion beam (FIB) assisted precursor decomposition. Afterward, the TEM lamella was prepared using a 30 keV Ga FIB with adapted currents. Its transfer to a three-post copper lift-out grid (Omniprobe) was done with a Kleindiek micromanipulator. To minimize sidewall damage, Ga ions with only 5 keV energy were used for final thinning of the TEM lamella to electron transparency. EDXS-based spectrum images were recorded at three locations for each sample with slightly different time, ranging from 480 to 633 s. The acquisition area for the Py(2 nm) and Py(10 nm) samples was 136×54 nm (1000×400 pixels) and 136×41 nm (1000×300 pixels), respectively.

Quantification of the element maps including bremsstrahlung background correction based on the physical TEM model, series fit peak deconvolution, and application of tabulated theoretical Cliff-Lorimer factors was done for the elements Pd ($L\alpha$ line), Y ($K\alpha$ line), Ni ($K\alpha$ line), and Fe ($K\alpha$ line) using the ESPRIT software version 1.9 (Bruker). The quantified element maps were then postprocessed in MATHCAD in the following manner: First, each element map (Pd, Y, Ni, and Fe) was converted into a matrix of atomic percent. It is known that electron irradiation during STEM-based analysis results in a release of oxygen in the SiO_2 layer [20] at the substrate, resulting in a decrease in the substrate thickness at the acquisition window and

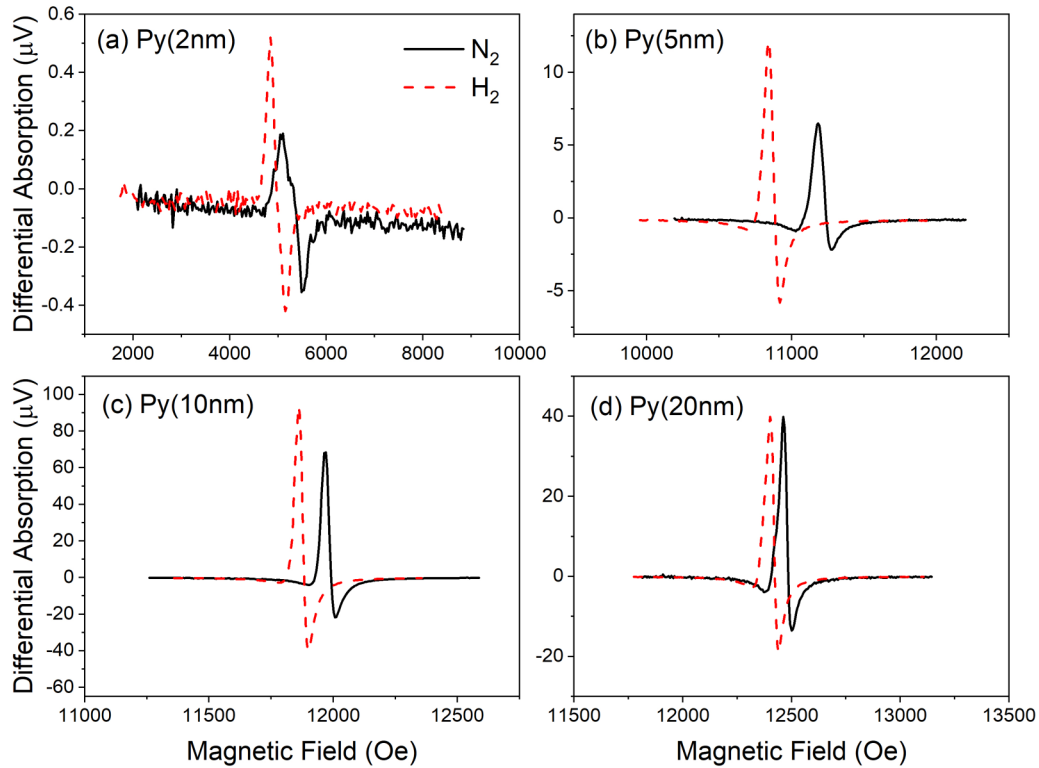


FIG. 1. FMR absorption curves for the Py(x nm)/Y(16 nm)/Pd(15 nm) samples with (a) $x = 2$ nm, (b) $x = 5$ nm, (c) $x = 10$ nm, (d) $x = 20$ nm, carried out for the N_2 atmosphere (black, solid line) and in H_2 atmosphere (red, dashed line) at (a) 6 GHz and (b)–(d) 10 GHz.

ultimately leading to a curvature in the resultant images. In order to account for this curvature, the “center of mass” of the counts for each column was calculated and plotted vs the horizontal pixel number for the Fe element map. Second, this curve was fitted with a second order polynomial, and each column was then shifted vertically to compensate for this parabolic curvature. All other element maps for a given image were compensated using the same polynomial fit as for Fe, since the same curvature should be present for all elements. Once flattened, the compositions in each row were averaged and plotted vs the cross-sectional thickness to obtain cross-sectional line profiles of the element maps, with the top surface corresponding to 0 nm. This was repeated for all three images for each sample piece, always using the Fe map to compensate the curvature. The three corresponding line profiles were then averaged. To do this averaging, the line profiles were shifted such that the three line profiles from the three images for each sample aligned. The Si/Fe interface was used as a reference for the alignment, and all the line profiles for the other elements were shifted by the same amount. Lastly, the line profiles of the hydrogenated and the virgin samples were overlaid. Again, we shifted all the virgin profiles such that the virgin and hydrogenated line profiles aligned, making sure to use the same shift for all elements, Pd, Y, Ni, and Fe.

III. RESULTS

In the presence of hydrogen gas, a down-field shifting of the out of plane FMR peak position as well as a narrowing of the FMR linewidth were observed, as seen in Fig. 1. Addi-

tionally, the FMR signal amplitude increases in the hydrogen atmosphere, which may be attributed to the narrowing of the FMR linewidth [21]. Both the FMR shift and linewidth narrowing were more pronounced for the thinner samples, which supports an interfacial effect. In this work the FMR peak position refers to the resonance field position of the field-swept FMR curves.

The asymmetric shape of the FMR peak, depicted in Fig. 1(a), is due to a double FMR peak. For the Py(2 nm) sample, depicted in Fig. 1(a), there appears a clear line splitting. Typically, we fit a single peak with the real part of the first derivative of a complex Lorentzian function, which results in a Lorentzian and an anti-Lorentzian term. In the case of the Py(2 nm) sample, we fitted all of the data with a double peak, i.e., two single peaks. The origin of the double peak is not understood, and even for the highest measurable frequency of 18 GHz, we observe the distorted line shape. The FMR peak position is ~ 9300 Oe at 18 GHz, which is above the saturating field given by OOP hysteresis measurements, suggesting the double peak is present even in a fully OOP-magnetized state. Such an FMR “doublet” has been investigated for two-layer garnet films [22,23], where one of the layers is magnetized in plane while the second layer forms partial OOP domains. However, for polycrystalline Py thin films, we do not expect partial domains to form in the ground state. Further investigations, which go beyond the scope of this study, would be required to validate this idea.

In order to monitor the absorption of hydrogen into the samples and the rate of the FMR peak shift, time-resolved measurements were carried out, as described in the previous section. Figure 2 shows how the FMR lock-in signal changes

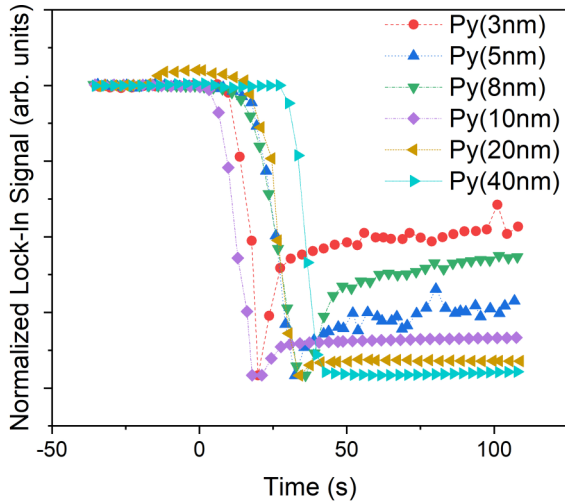


FIG. 2. Lock-in signal as a function of time measured at a set microwave driving frequency and externally applied magnetic field during the absorption of hydrogen into the Py(x nm)/Y(16 nm)/Pd(15 nm) samples, where the thickness of Py is given in the legend. The point $t = 0$ s corresponds to the swapping of atmospheres from 100% N_2 to 100% H_2 in the airtight chamber. The frequency and external field were set such that the lock-in probed the FMR peak between the two peaks of the anti-Lorentzian. The time-resolved data were normalized such that the drop was the same amplitude for all samples.

upon hydrogenation, i.e., after the airtight chamber was cycled from 100% N_2 to 100% H_2 at $t = 0$ s. After this time index, a steep drop of the signal can be observed for all samples, reaching a minimum between 10 and 50 s. The drop is associated with a rapid shifting of the FMR peak position, since the external magnetic field and the driving frequency have been set to fixed values for the time-dependent measurement. In Fig. 2, the steep drop was normalized for all samples, which enables comparison between the initial absorption rates for the various samples, given that their respective FMR curves have similar linewidths. One notices that the initial rapid absorption does not vary significantly between samples, which is expected, as the Py thicknesses should not impact the rate of hydrogen absorption. The Py(2 nm) sample was omitted in Fig. 2, as the FMR linewidth for this sample is much larger than for the other samples and, furthermore, the signal to noise ratio of the time-dependent curve for the Py(2 nm) was very low. In addition to the resonance shift, the narrowing of the FMR linewidth and increase in FMR amplitude [21] would be detected by the time-dependent measurements; however, in order to decouple these mechanisms, further time-dependent measurements would need to be carried out, which goes beyond the scope of this paper.

Similar, time-resolved measurements were carried out during the desorption of hydrogen from the samples and are shown in Fig. 3. The atmosphere in the chamber was cycled from 100% H_2 to 100% N_2 at $t = 0$ s and, similar to the absorption curves from Fig. 2, there was a fast initial response of the normalized lock-in signal followed by a slower tail. The time-resolved traces in Fig. 3 were normalized, which allows one to compare the shapes of the different

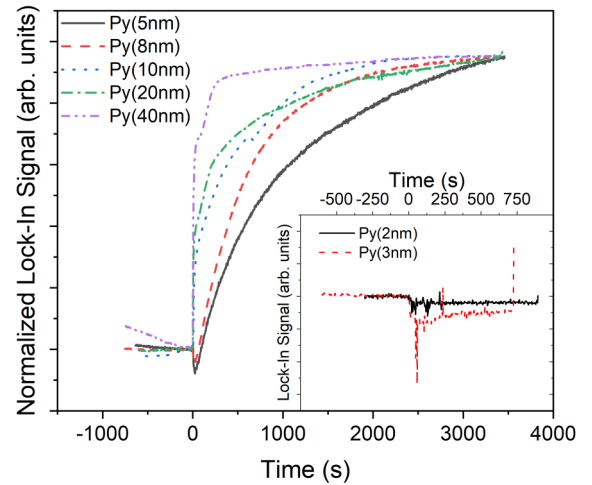


FIG. 3. Lock-in signal, as a function of time, measured at a set microwave driving frequency and externally applied magnetic field during the desorption of hydrogen from the Py(x nm)/Y(16 nm)/Pd(15 nm) samples, where the Py thickness is given in the legend. $t = 0$ s corresponds to the time the atmosphere in the airtight chamber was cycled from 100% H_2 to 100% N_2 . The frequency and external field were set such that the lock-in probed the FMR peak between the peaks of the anti-Lorentzian. The time-resolved data were normalized such that the total change for all samples was the same. Inset: non-normalized lock-in signal for the Py(2 nm) and Py(3 nm) samples during desorption.

curves. Thus, one notices that the rate of the initial desorption response depends on the thickness of the Py layer, with the thicker samples showing a faster response, as seen by the steeper slope at $t = 0$ s in Fig. 3. One also notices that the Py samples with thicknesses < 10 nm have an initial decrease in the time-resolved traces at $t = 0$ s. Given the shape of the out of plane FMR traces in our setup, one expects an increase in the time-resolved trace when the FMR peak position shifts to higher fields. We attribute the initial decrease in the time-resolved traces to an initial down-field shifting of the FMR peak position followed by the typical up-field shifting upon desorption.

A comparison of Figs. 2 and 3 shows that the initial rates of absorption are much quicker than the initial rates of desorption of hydrogen. Furthermore, all samples appear to have a similar initial absorption rate, whereas for desorption, the thicker samples show a faster initial desorption rate than the thinner samples.

Such time-dependent measurements have previously been employed in studies of hydrogen absorption in Pd/Co bilayer systems [8], where the time-dependent measurements were able to probe the entire hydrogen absorption process for the samples and thus could be used as an indicator of when the samples had reached maximum hydrogen saturation. However, the FMR linewidth of the Pd/Co bilayers was an order of magnitude larger than the FMR linewidth of the Pd/Y/Py samples studied in this paper. As a result, even though the FMR peak shifts were of similar magnitude for the Pd/Co and Pd/Y/Py samples, it was found that the FMR peak shifts by more than the FMR linewidth for the Pd/Y/Py samples due to the much smaller FMR linewidth in these samples. This is

not the case for the Pd/Co bilayers previously studied, and for such systems, the time-dependent measurement always probes the FMR curve between the two peaks of the differential FMR curve, which gives maximum sensitivity to changes in the FMR curve. For the Pd/Y/Py samples, the time-dependent measurement no longer probes the FMR curve between the two peaks of the differential FMR curve, once the FMR peak has shifted by more than the peak to peak linewidth. As a result, the sign of the slope as well as the measurement sensitivity changes. If the FMR peak continues to shift, then the sensitivity of this technique decreases further, eventually reaching zero when the time-resolved measurements probe the flat tail of the FMR curve, which is the case for our samples. As a result, it is not possible to get an exact indication of when the FMR peak has reached its steady state with these time-dependent measurements.

In order to account for this, the FMR peak position and FMR linewidth were measured at various times in 100% H₂ atmosphere by varying the magnetic field for a set frequency, as seen in Fig. 4 exemplarily shown for the Py(10 nm) sample. The FMR linewidth corresponds to the half width at half maximum (HWHM) of the differential FMR curves, taken by sweeping the applied magnetic field, and is measured in the magnetic field units Oe. The FMR measurement taken at a time of $t = 0$ min corresponds to the FMR in the virgin state, after which the atmosphere was cycled to 100% H₂. Figure 4(a) shows the raw FMR curves at various time points in the H₂ atmosphere labeled 1, 2, 3, and 4, which correspond to 0, 82, 262, and 361 min in H₂ atmosphere, respectively. From Fig. 4(b), it is evident that there is an initial rapid shift of the FMR peak position and then a long trailing tail, spanning for >5 h, where the FMR peak position continues to shift, but at a much lower rate. This slowly varying shift is difficult to detect with the time-dependent measurements shown in Fig. 2 due to the large loss of sensitivity when the FMR peak has shifted by more than the peak to peak linewidth. As a result, the time-dependent measurements in Fig. 2 are only useful for probing the samples' initial response to H₂ absorption.

By comparison, the FMR linewidth does not show such a slowly varying tail as compared to the FMR peak position, as can be seen from Fig. 4(c). The same was seen for all other Py thicknesses (not shown). This suggests that the change in the FMR linewidth and the change in the FMR peak position occur on different timescales and thus may have contributions from different mechanisms. For instance, if one associates the change in the FMR linewidth with a reordering of atoms at the Py/Y interface, then this suggests that the rearrangement occurs rapidly and that the slow shifting of the FMR peak position, seen for later times, occurs from a slower effect.

Figure 5 shows the behavior of the FMR curve during the desorption of H₂ for the Py(3 nm) sample, which was used as an example. Figure 5(a) shows the raw FMR curves for various time points during the desorption of H₂ from the sample. The curves are labeled 1, 2, and 3, corresponding to -27, 24, and 567 min, respectively, where the atmosphere in the chamber was cycled from 100% H₂ to 100% N₂ at $t = 0$ min. Thus, it is evident that the initial response of FMR to the desorption of hydrogen from the sample is a further down-field shifting of the FMR peak position as seen in Fig. 5(b). As the sample continues to desorb hydrogen, this shift in peak

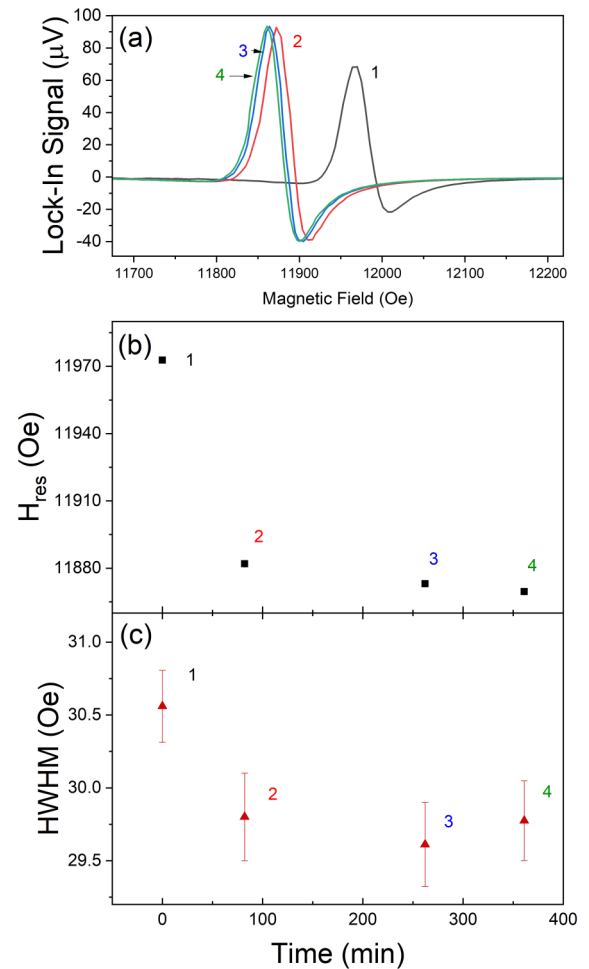


FIG. 4. (a) Raw FMR curves measured at 10 GHz at various time points during H₂ absorption for the Py(10 nm)/Y(16 nm)/Pd(15 nm) sample. (b) FMR peak position extracted from the corresponding FMR curves. (c) FMR half width at half maximum extracted from the corresponding FMR curves. The values for the resonance field in the tail regime have been fitted using an exponential decay function, $y = A + Be^{-t/\tau}$. The labels 1, 2, 3, and 4 correspond to 0, 82, 262, and 361 min in H₂ atmosphere for all panels.

position changes direction, and the peak shifts back up-field toward the virgin-state FMR peak position. Even after 567 min, the FMR peak did not return to its position as seen in the virgin state, which suggests that either the effects of hydrogen on the sample require timescales on the order of hours to days to return to their original virgin state or that hydrogen has an irreversible effect on the sample. The FMR HWHM shown in Fig. 5(c) does not show the odd behavior of first narrowing further and then starting to broaden again. Instead, even for short timescales of only 24 min in the N₂ atmosphere, it has already begun to broaden back toward the HWHM of the virgin state. This suggests that the FMR HWHM and FMR peak position act on different timescales for the desorption of H₂ as well.

We now turn to field-resolved FMR measurements obtained at various microwave driving frequencies. Such measurements were obtained in each atmosphere and for each sample. In H₂ atmosphere, the FMR curves were obtained in

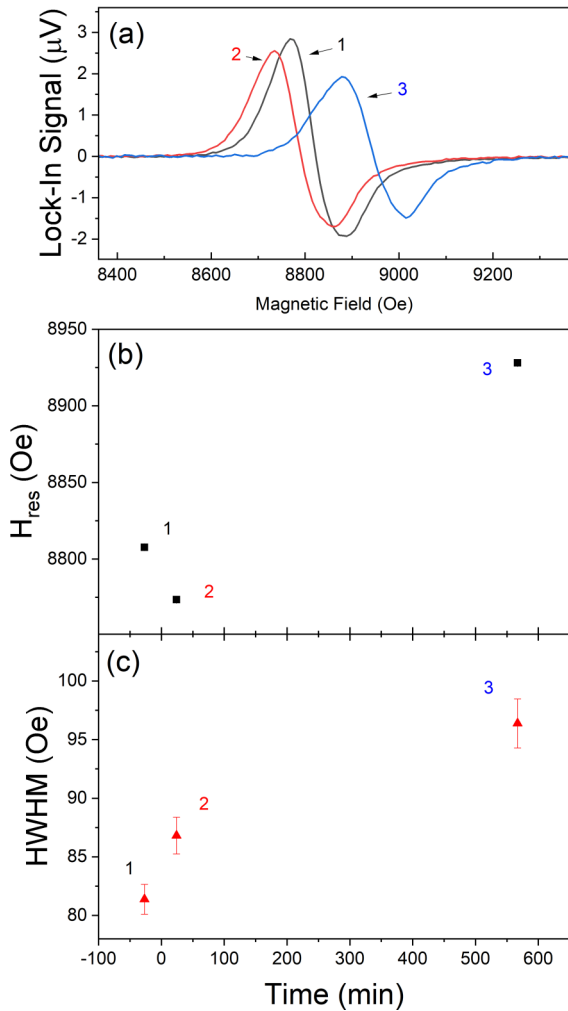


FIG. 5. (a) Raw FMR curves measured at 10 GHz at various time points during H_2 desorption for the Py(3 nm)/Y(16 nm)/Pd(15 nm) sample. (b) FMR peak position extracted from the corresponding FMR curves. (c) FMR half width at half maximum extracted from the corresponding FMR curves. The labels 1, 2, and 3 correspond to -27 , 24 , and 567 min, respectively, where $t = 0$ min corresponds to the time where the chamber was cycled from 100% H_2 to 100% N_2 .

the slowly varying tail regime, for example, with $t > 100$ min in Fig. 4(b) for the Py(10 nm) sample. As a consequence, due to the non-negligible, but very slow shifting of the FMR peak position during these measurements, a systematic error is expected, causing the FMR peak positions at higher frequencies to be shifted further than those measured at lower frequencies, which would be seen as an increased gyromagnetic ratio and effective magnetization. To correct for this, the points in the tail regime of Fig. 4(b) were fitted with an exponential decay function, $y = A + Be^{-t/\tau}$, and the corresponding fit was used to scale all of the FMR peak positions, measured at various frequencies and time points, to the longest time point. Such corrections were not required for the FMR linewidth, as it reaches a steady state much faster than the FMR peak position. The corrections were done this way for all samples.

In addition, the Py(2nm) sample was fitted with a double peak, and as a result, the time corrections were done individually for each peak. The first peak has a lower resonance

field, but broader FMR linewidth than the second peak. Both peaks shift down field in the presence of hydrogen gas, with the second peak shifting further than the first peak. The FMR linewidth, on the other hand, only narrows for the first peak. The narrowing is a direct consequence of a reduction in the inhomogeneous linewidth broadening, as seen by the downward shift of the HWHM vs frequency data in Fig. 6(b). If we assume the reduction in linewidth may be a result of interface clearing, as this would improve the homogeneity of this layer, then the magnetization dynamics underlying the peaks is affected differently by the state of the interface spins. Unfortunately, it is impossible to say anything about the origin of the double-peak character of the FMR response based on the evidence available to us so far. However, investigating the origins is outside the focus of the present paper; therefore we leave this aspect for a future study.

For comparison, the resonance frequency vs magnetic field for the Py(10 nm) sample is displayed in Fig. 7. From Figs. 6 and 7, it is evident that the effects of hydrogen are more pronounced for the Py(2 nm) sample than the Py(10 nm) sample, as seen from the larger shift in the FMR peak position as well as the larger reduction in the FMR linewidth for the thinner sample. The FMR peak positions in hydrogen-loaded samples [red circles in Figs. 6(a), 6(c), and 7(a)] have been scaled to the same time, as discussed earlier, in order to remove systematic errors from the slow shifting of the FMR peak position during each frequency-dependent measurement. The scaling was not performed for the FMR peak positions after the desorption of hydrogen [blue triangles in Figs. 6(a), 6(c), and 7(a)], as not enough FMR measurements were carried out at different times for the same frequency during the desorption of hydrogen from the samples. This results in a deviation of the slope of the microwave frequency vs FMR peak position from the true slope and systematic errors in the extraction of the gyromagnetic ratio (γ) and the effective magnetization ($4\pi M_{\text{eff}}$). Thus, the extracted parameters in the desorbed sample are not included in this study. Looking at the highest frequencies for the Py(2 nm) and Py(10 nm) samples (13.5 and 13 GHz, measured ~ 12 h, 35 min and ~ 15 h, 2 min after the chamber was flushed with 100% N_2 , respectively) one notices that the FMR peak position did not fully reverse back to its virgin state. On the other hand, the FMR linewidth shows a much more reversible process than the FMR peak position at the same frequencies. Thus, as for the hydrogen absorption, the FMR linewidth reacts much faster to hydrogen desorption than the FMR peak position.

For all samples, the effective magnetization ($4\pi M_{\text{eff}}$) and gyromagnetic ratio (γ) were extracted from linear fits of the resonance fields taken at different frequencies, to the well-known out of plane Kittel equation [24] $\omega = \gamma(H_{\text{res}} - 4\pi M_{\text{eff}})$, where $4\pi M_{\text{eff}} = 4\pi M_s - H_u$, and H_u is the effective field due to perpendicular magnetic anisotropy (PMA). Note, in this formalism of the Kittel equation, the demagnetizing field has already been accounted for during its derivation, and thus H_u corresponds solely to the effective field of PMA. Due to the nature of FMR, it is not possible to decouple the contributions of the saturation magnetization and the effective anisotropy field to the effective magnetization. In order to account for this, magnetometry was carried out on virgin pieces of the samples in order to extract $4\pi M_s$.

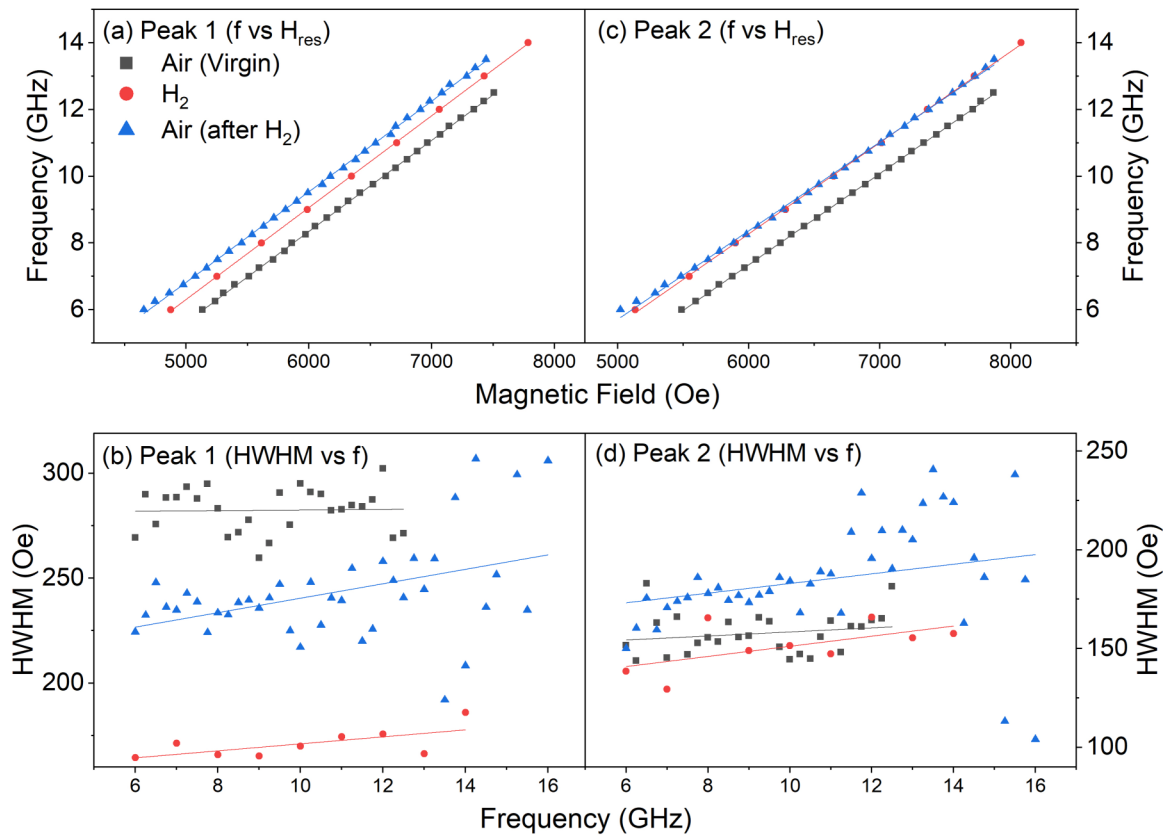


FIG. 6. Magnetic field swept out of plane FMR results for the Py(2 nm)/Y(16 nm)/Pd(15 nm) sample when fitted with a double peak. (a,c) show the FMR frequency dependence on the externally applied magnetic field for the first and second fitted peak, respectively. (b,d) show the FMR linewidth dependence on the microwave driving frequency for the first and second fitted peak, respectively. Black squares: FMR measurements carried out on the virgin sample in air. Red circles: FMR measurements carried out in 100% H₂ atmosphere (scaled to the same time). Blue triangles: FMR measurements carried out in air after >20 min of flushing with 100% N₂ (unscaled raw results). Solid lines: linear fits to the data of the same color.

In-plane and out of plane magnetic hysteresis loops, obtained via vibrating sample magnetometry for the Py(2 nm) and Py(10 nm) samples, are provided exemplarily in Fig. 8.

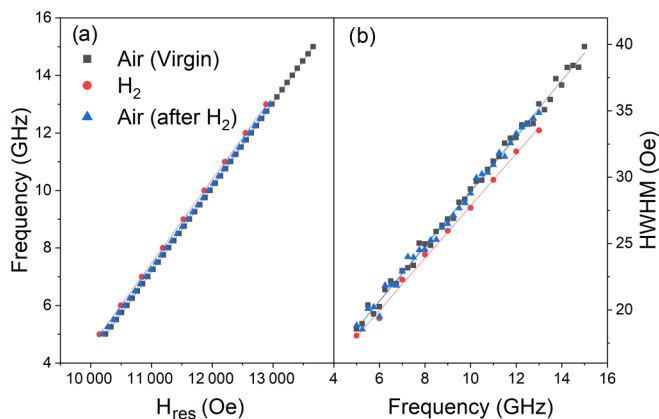


FIG. 7. Out of plane FMR data for the Py(10 nm)/Y(16 nm)/Pd(15 nm) sample. (a) FMR frequency vs resonance field. (b) FMR linewidth vs FMR driving frequency. Black squares: FMR measurements carried out on the virgin sample in air. Red circles: FMR measurements carried out in 100% H₂ atmosphere (scaled to the same time). Blue triangles: FMR measurements carried out in air after flushing with 100% N₂ (unscaled raw results).

The magnetization ($4\pi M$) from hysteresis loops was obtained by dividing the magnetic moment measured from vibrating sample magnetometry by the sample area and the nominal film thickness, i.e., the nominal film volume. The results in emu/cm³ were then multiplied by 4π in order to obtain the magnetization in gauss. From the squareness of the in-plane and out of plane hysteresis loops, it is clear that the easy axis of magnetization points in the sample plane and the hard axis points out of the sample plane. The same behavior was present for all samples in the series. From the hysteresis loops, there is no clear evidence of interface PMA at the Py/Y interface and the presence of interface PMA is inferred from the FMR data as discussed below.

The areal magnetization ($4\pi M_s \times t_{\text{Py}}$) vs the nominal Py thickness (t_{Py}) is shown by the inset in Fig. 9. Fitting these data with a linear function gives a magnetic dead layer of 0.9 nm, determined from the x intercept. The data point for the Py(8 nm) sample is omitted in the linear fits, as it lies significantly below the trend and inclusion of this point results in a dead layer of 1.1 nm. This is not physical, as it suggests that the Py(1 nm) sample is entirely dead and has no magnetic contribution; however, this cannot be the case, as a magnetic signal is observed from hysteresis loops for this sample. Assuming the magnetic dead layer is constant for all Py thicknesses, the effective ferromagnetic layer thickness

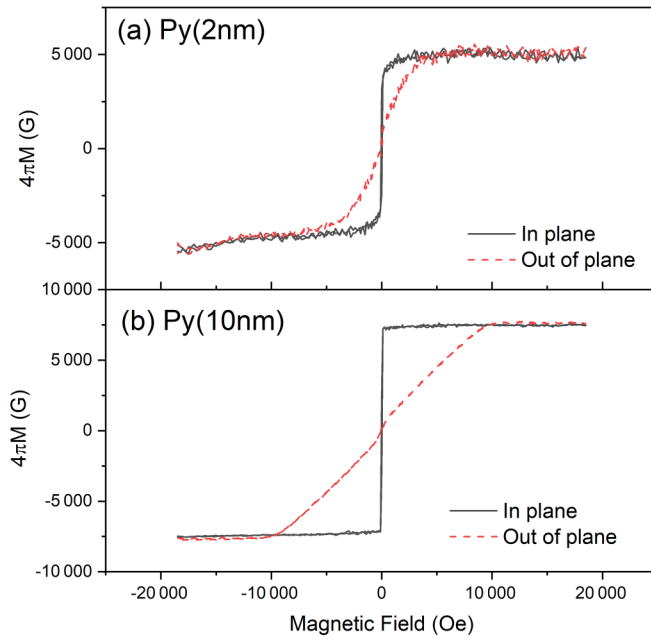


FIG. 8. In-plane (black solid line) and out of plane (red dashed line) hysteresis loops for the (a) Py(2 nm) and (b) Py(10 nm) samples. The magnetization $4\pi M$ in the figures was obtained by dividing the magnetic moment (as measured by VSM) by the volume of the ferromagnetic layer, while the thickness of the ferromagnetic layer was taken as the nominal one, 2 and 10 nm for (a), (b) respectively.

($t_{\text{eff}} = t_{\text{Py}} - t_{\text{dead}}$), which contributes to the magnetization, is actually smaller than the nominal Py thickness (t_{Py}). Introducing the magnetic dead layer of 0.9 nm into the results from VSM, an approximate constant $4\pi M_s$ for all sample thicknesses is obtained, which is depicted by the purple diamonds in Fig. 9. The origin of the magnetic dead layer may be explained as

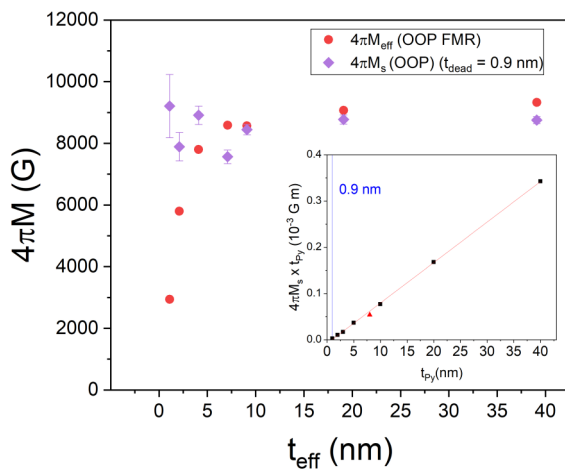


FIG. 9. Saturation magnetization extracted from magnetometry as a function of the effective ferromagnetic layer thickness. Purple diamonds: $4\pi M_s$ extracted by introducing a dead layer of 0.9 nm. Red circles: effective magnetization from OOP FMR. Inset: Py thickness dependence of areal magnetization ($4\pi M_s \times t_{\text{Py}}$). The magnetic dead layer thickness is indicated by a blue vertical line. The red triangle was omitted in the red linear fit.

either stemming from oxidation of the Fe atoms at the substrate/Py interface [25], due to the thermally oxidized SiO₂ substrate, or as a result of intermixing at the Py/Y interface.

For the thinner samples, $4\pi M_{\text{eff}}$, extracted from OOP FMR, is smaller than $4\pi M_s$, which is expected when dealing with an interfacial PMA (iPMA) since the iPMA contribution subtracts from the saturation magnetization: $4\pi M_{\text{eff}} = 4\pi M_s - H_u$. As the thickness of the sample is increased, the effects of iPMA decrease due to its interfacial nature, and one expects $4\pi M_{\text{eff}}$ and $4\pi M_s$ to converge. This convergence is not observed, and one sees that $4\pi M_{\text{eff}}$, shown by the red circles in Fig. 9, becomes larger than $4\pi M_s$ as the Py thickness is increased. For the Py(40 nm) sample, it is expected that the iPMA contribution to $4\pi M_{\text{eff}}$ is negligible, supported by the flattening of the $4\pi M_{\text{eff}}$ vs t_{eff} data. Thus, an extra contribution must be present which has a sign opposite to the iPMA contribution, resulting in an increase in $4\pi M_{\text{eff}}$. It is believed that this contribution arises from a bulk easy-plane anisotropy which minimizes the energy when the magnetic moments align themselves in any direction in the plane of the sample. As a result, the modified effective magnetization becomes $4\pi M_{\text{eff}} = 4\pi M_s - H_u + H_{\text{ep}}$, where H_{ep} is the effective field due to the bulk easy-plane anisotropy.

In Fig. 10, the extracted FMR parameters are plotted vs the inverse Py thickness. For the Py(2 nm) sample, which was fitted with a double FMR peak, only the data extracted from the first peak are shown for ease of viewing, with the exception of the effective magnetization and inhomogeneous linewidth broadening, for which the second peak is shown in the inset of Figs. 10(a) and 10(d), respectively. Plotting the extracted $4\pi M_{\text{eff}}$ vs the inverse of the effective Py thickness results in a downward linear trend, as seen in Fig. 10(a), indicative of an interface effect such as the discussed iPMA. The linear behavior suggests that the easy-plane contribution must either be constant for all Py thicknesses or also scale linearly with the inverse Py thickness. If there is a linear scaling of the easy-plane anisotropy, it is indistinguishable from the interface PMA contribution (essentially just partly compensating the effective PMA field), and the only contribution that can be extracted from the experiment is the constant one. In either case, any linear contributions for the Py(40 nm) sample should be negligible, and we expect only a constant contribution from the easy-plane anisotropy at this thickness. This constant easy-plane contribution extracted for Py(40 nm) is approximately 575 Oe. In addition, in-plane angle-resolved FMR measurements were also carried out on the Py(40 nm) sample. The in-plane uniaxial anisotropy was found to be less than 20 Oe, which cannot explain the large extra contribution of 575 Oe. Thus, a bulk easy-plane anisotropy remains the most appropriate explanation. In the presence of hydrogen gas, $4\pi M_{\text{eff}}$ decreases, a behavior that is more pronounced for thinner Py thicknesses, suggesting that the presence of hydrogen gas predominantly affects the interface. This is expected, as hydrogen is not soluble in Py at ambient conditions and thus should not impact the bulk of the ferromagnetic layer. Due to the slow reversibility of the FMR peak position, we do not show the extracted $4\pi M_{\text{eff}}$ and γ after hydrogen desorption.

Previous works focusing on Co/Pd bilayer films [6,7,19] have found an increase in $4\pi M_{\text{eff}}$ in the presence of hydrogen gas, which is opposite to what is observed in this study. For

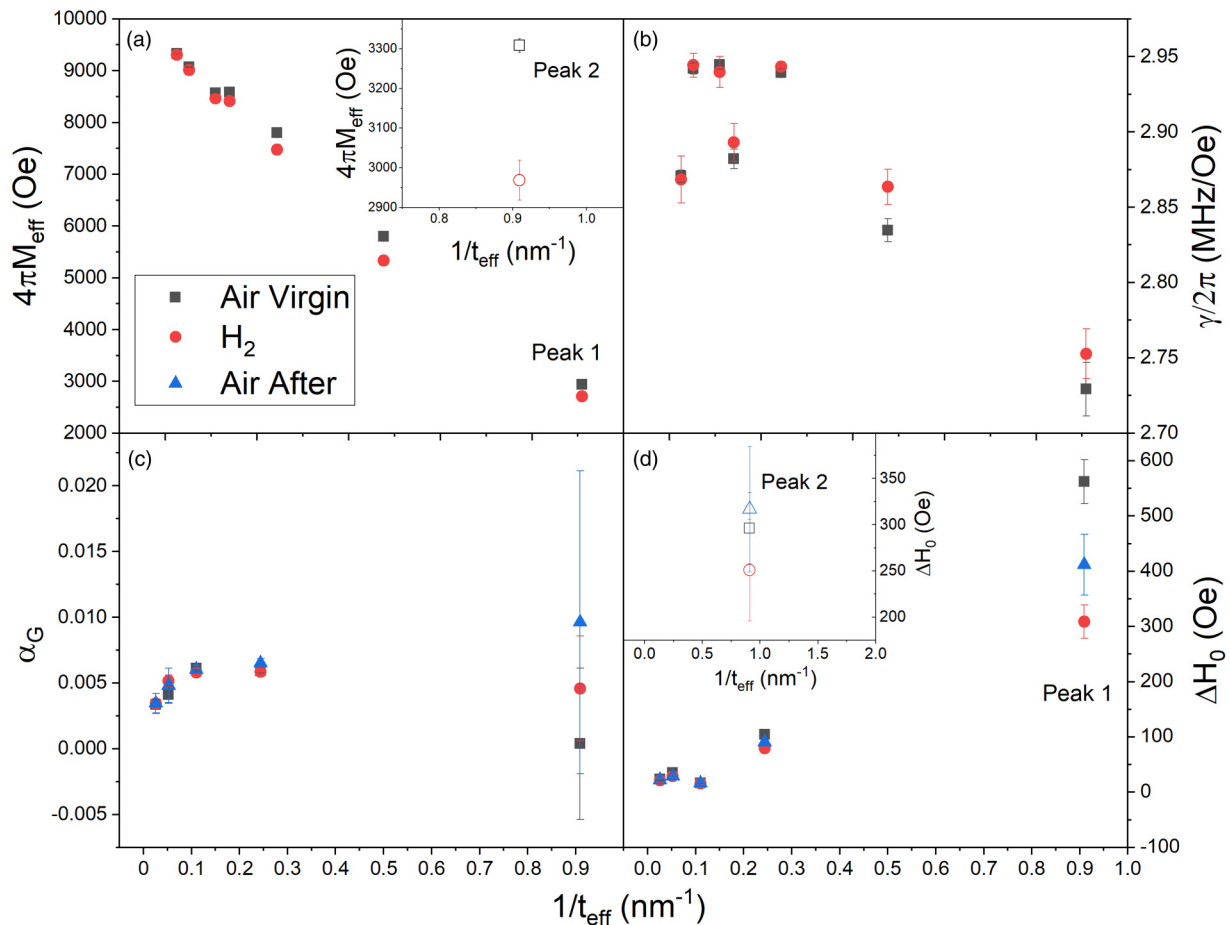


FIG. 10. Extracted parameters from FMR measurements plotted vs the inverse Py thickness. (a) Effective magnetization ($4\pi M_{\text{eff}}$). (b) Reduced gyromagnetic ratio ($\gamma/2\pi$). (c) Effective Gilbert damping constant (α_G). (d) Inhomogeneous linewidth broadening (ΔH_0). Inset of (a,d): effective magnetization and inhomogeneous linewidth broadening of second fitted FMR peak for Py(2 nm), respectively. Black squares: extracted from virgin sample in air. Red circles: extracted from sample in 100% H_2 after ~ 1 h of H_2 absorption. Blue triangles: extracted from sample after hydrogen was allowed to desorb for at least 30 min.

the Co/Pd films, the increase in $4\pi M_{\text{eff}}$ was explained as being caused by a decrease in the perpendicular magnetic anisotropy present at the interface, caused by a change in the spin-orbit coupling between the Pd and Co atoms [6,26]. However, the opposite effect may occur in our Py/Y/Pd samples, namely, that the perpendicular magnetic anisotropy increases in the presence of hydrogen gas. A recent theoretical study found that the Co/Pd system is expected to have a decrease in PMA in the presence of hydrogen, whereas an Fe/V system is expected to have an increase in PMA [26]. Thus, the Py/Y interface may act similarly to the Fe/V interface, resulting in an increase in PMA and ultimately down-field shifting of the FMR peak position in the OOP geometry.

Figure 11 shows that the change in $4\pi M_{\text{eff}}$ linearly depends on the inverse Py thickness, with the exception of the Py(2 nm) sample. The anomalous behavior of the Py(2 nm) sample is not fully understood, but it is speculated that this is a result of its thin nature, potentially also resulting in the presence of the double-peak response. (Indeed, the thickness of the magnetic layer corrected to the presence of the dead layer is just 1.1 nm for this sample.) Ignoring this obvious outlier, an overall linear behavior of the change in $4\pi M_{\text{eff}}$ is observed,

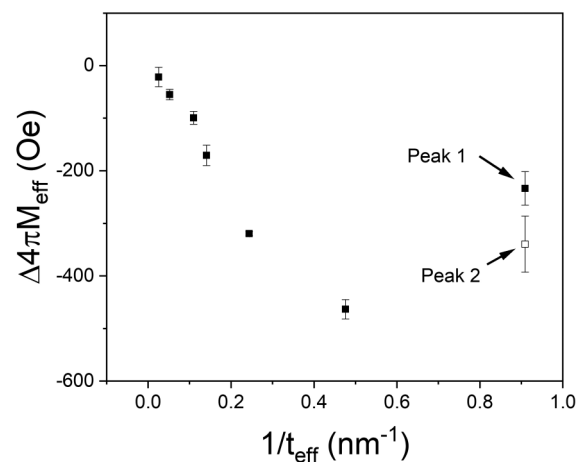


FIG. 11. Change in $4\pi M_{\text{eff}}$ between virgin and hydrogenated states as a function of the effective inverse Py thickness. Open points correspond to the second fitted peak for the Py(2 nm) sample. The extra contribution to $4\pi M_{\text{eff}}$ of 575 Oe was not subtracted in the data.

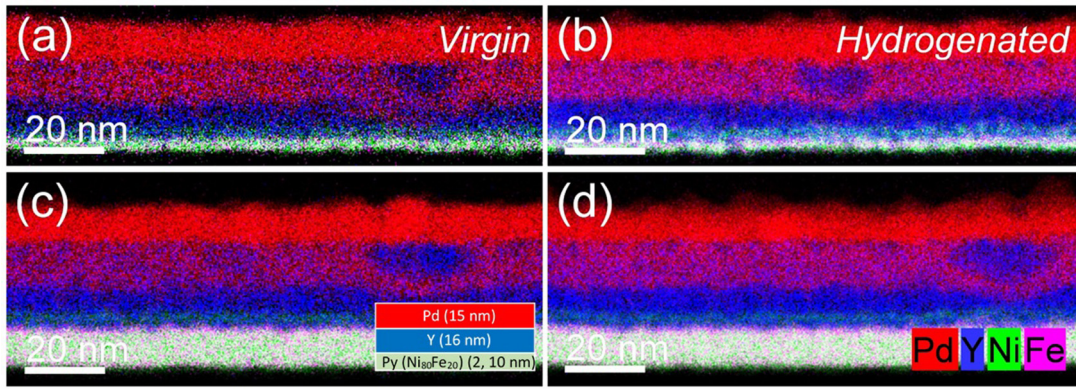


FIG. 12. Superimposed EDXS-based element distributions (Pd: red; Y: blue; Fe: magenta; Ni: green) of the virgin state (left panels) and after samples have gone through one hydrogenation cycle [i.e., air (100% N₂)–100% H₂–100% N₂] (right panels). (a,b) Py(2 nm)/Y(16 nm)/Pd(15 nm) sample. (c,d) Py(10 nm)/Y(16 nm)/Pd(15 nm) sample. Inset of (c): the nominal layer ordering for all samples.

which confirms that the effects of hydrogen act as an interface effect on the FMR.

Plotting the HWHM vs the frequency allows for the extraction of the effective Gilbert damping constant (α_G) as well as the inhomogeneous linewidth broadening (ΔH_0) by fitting with the equation [27] $\text{HWHM}(f) = \frac{2\pi\alpha_G}{\gamma}f + \frac{\Delta H_0}{2}$, where f is the microwave frequency. Fits for the Py(3 nm) and Py(8 nm) samples were omitted due to an oscillatory behavior in the FMR linewidth when plotted vs the microwave frequency. In Figs. 10(c) and 10(d), one notices that the main contribution to the FMR linewidth narrowing in the presence of hydrogen gas arises from a reduction in ΔH_0 , which may be associated with a reduction of surface roughness [28] at the Py/Y interface. The α_G parameter does not change more than the error margin in any of the samples, which suggests that the presence of hydrogen has no significant effect on the homogeneous contribution to the linewidth, such as spin pumping.

The hydrogen absorption in a thin film may result in the rearrangement of atoms [29] and that this can result in reduction of the intermixing present at the interface of two metals [14], which could be the reason for reduced surface roughness at the Py/Y interface in our samples. It is known that the surface roughness may directly affect the inhomogeneous linewidth broadening [28] and thus may explain the reduced inhomogeneous linewidth broadening seen in the presence of H₂. Additionally, the surface roughness may impact the homogeneity of PMA in the thin films [30]. We speculate that the iPMA along the Py/Y interface may have some inhomogeneity in magnitude or orientation and, as a result, the average iPMA contribution from the entire interface will be smaller than the localized maximum iPMA strength. With an improved surface roughness in H₂, this iPMA contribution may become more homogeneous along the Py/Y interface, resulting in a stronger average iPMA contribution. The larger iPMA would result in a reduced $4\pi M_{\text{eff}}$, which is observed in the experimental FMR measurements. This change in $4\pi M_{\text{eff}}$ should happen on the same timescale as the change in the FMR linewidth, as they stem from the same improvement of surface roughness at the Py/Y interface. However, once the Py/Y interface has reached maximum homogeneity, there may be a continual increase of iPMA due to a change in the spin-orbit coupling, as has been previously

speculated [6], leading to the slowly varying tail of the FMR peak position.

In order to better understand the behavior of the atoms at the Py/Y interface in the presence of hydrogen, EDXS-based spectrum images were obtained for a virgin and hydrogenated sample piece of the Py(2 nm) and Py(10 nm) samples. Examples of the obtained element distributions are displayed in Fig. 12. For the Py(2 nm) as well as the Py(10 nm) sample, Pd and Y create a significant intermixing layer, which may be associated to a favorable enthalpy of mixing [31,32]. It should be noted that in this Y-Pd intermixing layer, Y appears to be locally oxidized (for clarity, the O signal is not shown here), and that the presence of this Y oxide displaces Pd atoms in that area, resulting in pockets of Pd deficit. These local Pd cavities result in a broadening of the corresponding Pd line profiles, thus, if there is a different degree of oxidation in the virgin and hydrogenated states, this may be picked up as a difference between the virgin and hydrogenated states in the Pd curves. In order to account for this, we avoided specimen regions which displayed significant Pd cavities when creating the element line profiles, which are presented in Figs. 13 and 14.

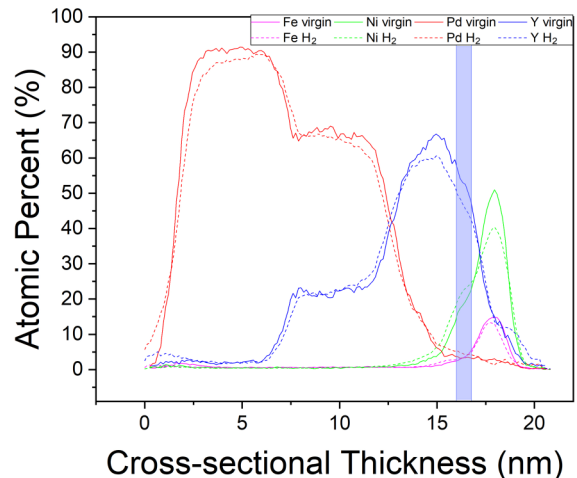


FIG. 13. Cross-sectional line profiles of the average atomic percent per pixel for the Py(2 nm)/Y(16 nm)/Pd(15 nm) samples. Solid lines: virgin sample, dashed lines: Hydrogenated sample. Red: Pd; blue: Y; green: Ni; magenta: Fe. The colors are the same as in Fig. 12.

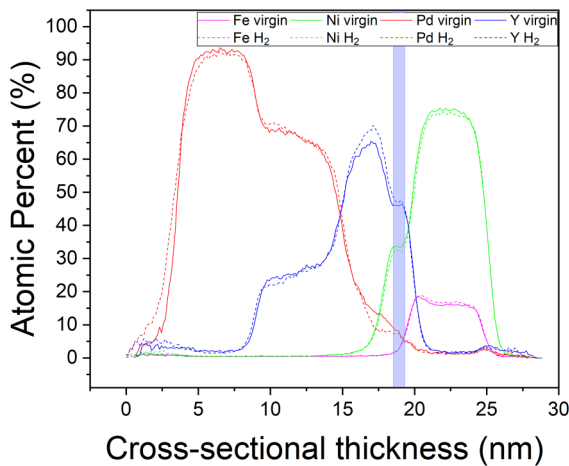


FIG. 14. Cross-sectional line profiles of the average atomic percent per pixel for the Py(10 nm)/Y(16 nm)/Pd(15 nm) samples. Solid lines: virgin sample; dashed lines: hydrogenated sample. Red: Pd; blue: Y; green: Ni; magenta: Fe. The colors are the same as in Fig. 12.

Both the Py(2 nm) and Py(10 nm) samples show a Ni-enriched area near the Py/Y interface, where the Ni/Fe ratio differs from that in the bulk Py layer, as highlighted by the blue-shaded regions in Figs. 13 and 14. It is known that Ni has a lower saturation magnetization and larger magnetic damping than Fe. Thus, this Ni-enriched region is expected to have a weaker contribution to the FMR signal. Besides the Ni enrichment in Py, for the Py(2 nm) sample, Y and Py intermix almost entirely throughout the Py layer via pinholes present in the Py layer. For the Py(10 nm) sample, this is not the case, as can be seen in Figs. 12 and 14, and there remains a pure Py bulk layer.

As expected from the element maps in Fig. 12, the line profiles in Figs. 13 and 14 show no significant differences between the virgin and hydrogenated states. Consequently, the TEM results suggest that if any atomic movement is present during the hydrogenation, this reverses after the desorption of hydrogen, which is consistent with the observed reversibility of the FMR linewidth. Thus, we speculate that during the absorption of hydrogen into the samples, the atoms at the Py/Y interface rearrange, resulting in a smoother Py/Y interface, which leads to a significant reduction of ΔH_0 as well as a

more homogeneous iPMA. During the desorption of hydrogen from the samples, the atoms may rearrange again and return to a similar intermixed state as for the virgin case. This rearrangement is much more pronounced for the thinner samples, as the interface layer acts as a much larger percentage of the whole ferromagnetic layer, resulting in a larger reduction of the linewidth for the thinnest samples.

IV. CONCLUSION

It was shown that hydrogen absorption in a series of Py(x nm)/Y(16 nm)/Pd(15 nm) samples with $x = 2, 3, 5, 8, 10, 20, 40$ nm results in a reduction of the effective magnetization ($4\pi M_{\text{eff}}$) as well as a narrowing of the FMR linewidth. The origin of the reduction of $4\pi M_{\text{eff}}$ is explained as an increase in the interfacial PMA at the Py/Y interface. The reduction in the FMR linewidth has been shown to originate from a reduction in the inhomogeneous linewidth broadening (ΔH_0), which is believed to stem from a reduction in the Py/Y interfacial roughness in the presence of hydrogen gas. STEM-based element analysis showed no irreversible movement of atoms in the samples between the virgin and hydrogenated states, which is consistent with the reversible behavior of the FMR linewidth. Additionally, the reductions in $4\pi M_{\text{eff}}$ and ΔH_0 are more pronounced for the thinner samples, which supports the notion of an interface effect during hydrogenation.

ACKNOWLEDGMENTS

A Research Collaboration Award from the University of Western Australia (UWA) is acknowledged. C.W. acknowledges his Research Training Program stipend from UWA. The authors thank A. Kunz and R. Aniol for TEM specimen preparation. Furthermore, the use of the HZDR Ion Beam Center TEM facilities and the funding of TEM Talos by the German Federal Ministry of Education and Research (BMBF; Grant No. 03SF0451) in the framework of HEMCP are acknowledged. The authors acknowledge the facilities, and the scientific and technical assistance of Microscopy Australia at the Centre for Microscopy, Characterisation & Analysis, The University of Western Australia, a facility funded by the University, State and Commonwealth Governments.

- [1] B. D. Adams and A. Chen, The role of palladium in a hydrogen economy, *Mater. Today* **14**, 282 (2011).
- [2] G. Marbán and T. Valdés-Solís, Towards the hydrogen economy? *Int. J. Hydrogen Energy* **32**, 1625 (2007).
- [3] A. L. Mejdell, M. Jøndahl, T. A. Peters, R. Bredesen, and H. J. Venvik, Effects of CO and CO₂ on hydrogen permeation through a $\sim 3 \mu\text{m}$ Pd/Ag 23 wt.% membrane employed in a microchannel membrane configuration, *Sep. Purif. Technol.* **68**, 178 (2009).
- [4] T. Hübert, L. Boon-Brett, G. Black, and U. Banach, Hydrogen sensors—a review, *Sens. Actuators, B* **157**, 329 (2011).
- [5] T. Hübert, L. Boon-Brett, V. Palmisano, and M. A. Bader, Developments in gas sensor technology for hydrogen safety, *Int. J. Hydrogen Energy* **39**, 20474 (2014).
- [6] C. S. Chang, M. Kostylev, and E. Ivanov, Metallic spintronic thin film as a hydrogen sensor, *Appl. Phys. Lett.* **102**, 142405 (2013).
- [7] C. Lueng, P. J. Metaxas, and M. Kostylev, Pd/Co bi-layer films for microwave-frequency hydrogen gas sensing applications, in *COMMAD 2014 Conference Proceedings, 2014 Conference on Optoelectronic and Microelectronic Materials and Devices* (Wiley-IEEE, New York, 2014), pp. 27–29.
- [8] C. Lueng, P. J. Metaxas, M. Sushruth, and M. Kostylev, Adjustable sensitivity for hydrogen gas sensing using perpendicular-to-plane ferromagnetic resonance in Pd/Co bi-layer films, *Int. J. Hydrogen Energy* **42**, 3407 (2017).
- [9] C. Lueng, P. Lupo, P. J. Metaxas, M. Kostylev, and A. O. Adeyeye, Nanopatterning-enhanced sensitivity and response

- time of dynamic palladium/cobalt/palladium hydrogen gas sensors, *Adv. Mater. Technol.* **1**, 1600097 (2016).
- [10] C. Lueng, F. Zighem, D. Faurie, and M. Kostylev, Ferromagnetic resonance investigation of physical origins of modification of the perpendicular magnetic anisotropy in Pd/Co layered films in the presence of hydrogen gas, *J. Appl. Phys.* **122**, 163901 (2017).
- [11] K. Munbodh, F. A. Perez, and D. Lederman, Changes in magnetic properties of Co/Pd multilayers induced by hydrogen absorption, *J. Appl. Phys.* **111**, 123919 (2012).
- [12] K. Munbodh, F. A. Perez, C. Keenan, D. Lederman, M. Zhernenkov, and M. R. Fitzsimmons, Effects of hydrogen/deuterium absorption on the magnetic properties of Co/Pd multilayers, *Phys. Rev. B* **83**, 094432 (2011).
- [13] Y. Kamada, A. Itoh, D. Takama, and M. Yamamoto, Effects of hydrogenation on the structure, transport, and magnetic properties of multilayers composed of transition metals and rare-earth metals, *Trans. Magn. Soc. Jpn.* **2**, 69 (2002).
- [14] Y. Endo, D. Takama, M. Yamamoto, T. Suenobu, and S. Fukuzumi, Change of interlayer exchange coupling in Fe/Y multilayers by hydrogenation, *Jpn. J. Appl. Phys.* **44**, 158 (2005).
- [15] Y. Endo, D. Takama, M. Yamamoto, T. Suenobu, and S. Fukuzumi, Interlayer exchange coupling of Fe/Y multilayers, *Jpn. J. Appl. Phys.* **42**, L291 (2003).
- [16] Y. Endo, K. Matsuura, M. Yamamoto, Y. Kamada, A. Itoh, T. Suenobu, and S. Fukuzumi, Effects of hydrogenation on structure and magnetic properties of Fe/La multilayers, *Sci. Technol. Adv. Mater.* **5**, 95 (2004).
- [17] Y. Tserkovnyak, A. Brataas, and G. E. W. Bauer, Enhanced Gilbert Damping in Thin Ferromagnetic Films, *Phys. Rev. Lett.* **88**, 117601 (2002).
- [18] Y. Tserkovnyak, A. Brataas, and G. E. W. Bauer, Spin pumping and magnetization dynamics in metallic multilayers, *Phys. Rev. B* **66**, 224403 (2002).
- [19] C. Lueng, P. J. Metaxas, and M. Kostylev, Sensitivity enhancement of a Pd/Co bilayer film for hydrogen gas sensing using a perpendicular-to-plane ferromagnetic resonance configuration, *IEEE Trans. Magn.* **52**, 1 (2016).
- [20] K. K. Neelisetty, X. Mu, S. Gutsch, A. Vahl, A. Molinari, F. von Seggern, M. Hansen, T. Scherer, M. Zacharias, L. Kienle, V. K. Chakravadhanula, and C. Kübel, Electron beam effects on oxide thin films—structure and electrical property correlations, *Microsc. Microanal.* **25**, 592 (2019).
- [21] T. A. Schefer and M. Kostylev, Effect of hydrogen gas on the FMR absorption amplitude of Pd/Co layered films, *IEEE Trans. Magn.* **54**, 1 (2018).
- [22] V. S. Dellalov, A. I. Linnik, V. F. Shkar, and S. V. Yampolskii, FMR peculiarities in two-layer bi-doped garnet films, *J. Magn. Magn. Mater.* **172**, 74 (1997).
- [23] A. M. Grishin, V. S. Dellalov, E. I. Nikolaev, V. F. Shkar', and S. V. Yampol'skii, FMR doublet in two-layer iron garnet films, *Zh. Eksp. Teor. Fiz.* **104**, 3450 (1993) [*JETP* **77**, 636 (1993)].
- [24] C. Kittel, Ferromagnetic resonance, *J. Phys. Radium* **12**, 291 (1951).
- [25] Q. Liu, X. Chen, J.-Y. Zhang, M. Yang, X.-J. Li, S.-L. Jiang, Y.-W. Liu, Y. Cao, Z.-L. Wu, C. Feng, L. Ding, and G.-H. Yu, Effects of interfacial Fe electronic structures on magnetic and electronic transport properties in oxide/NiFe/oxide heterostructures, *Appl. Surf. Sci.* **349**, 524 (2015).
- [26] K. Klyukin, G. Beach, and B. Yildiz, Hydrogen tunes magnetic anisotropy by affecting local hybridization at the interface of a ferromagnet with nonmagnetic metals, *Phys. Rev. Mater.* **4**, 104416 (2020).
- [27] T. D. Rossing, Resonance linewidth and anisotropy variation in thin films, *J. Appl. Phys.* **34**, 995 (1963).
- [28] J. M. Shaw, H. T. Nembach, and T. J. Silva, Roughness induced magnetic inhomogeneity in Co/Ni multilayers: Ferromagnetic resonance and switching properties in nanostructures, *J. Appl. Phys.* **108**, 093922 (2010).
- [29] H. Maletta, Ch. Rehm, F. Klose, M. Fieber-Erdmann, and E. Holub-Krappe, Anomalous effects of hydrogen absorption in Nb films, *J. Magn. Magn. Mater.* **240**, 475 (2002).
- [30] J. M. Shaw, H. T. Nembach, and T. J. Silva, Resolving the controversy of a possible relationship between perpendicular magnetic anisotropy and the magnetic damping parameter, *Appl. Phys. Lett.* **105**, 062406 (2014).
- [31] M.-Y. Wu, Q.-S. Huang, K. Le Guen, V. Ilakovac, B.-X. Li, Z.-S. Wang, A. Giglia, J.-P. Rueff, and P. Jonnard, Characterization of Pd/Y multilayers with B₄C barrier layers using GIXR and x-ray standing wave enhanced HAXPES, *J. Synchrotron Radiat.* **25**, 1417 (2018).
- [32] A. R. Miedema, P. F. de Châtel, and F. R. de Boer, Cohesion in alloys—fundamentals of a semi-empirical model, *Phys. B+C (Amsterdam)* **100**, 1 (1980).